

Article

# Solar Energy Dependent Supercapacitor System with ANFIS Controller for Auxiliary Load of Electric Vehicles

Ataur Rahman <sup>1</sup>, Kyaw Myo Aung <sup>1</sup>, Sany Ihsan <sup>1</sup>, Raja Mazuir Raja Ahsan Shah <sup>2,\*</sup>, Mansour Al Qubeissi <sup>3,\*</sup> and Mohannad T. Aljarrah <sup>2,4</sup>

<sup>1</sup> Department of Mechanical Engineering, International Islamic University Malaysia, Kuala Lumpur 53100, Malaysia

<sup>2</sup> College of Engineering Technology, University of Doha for Science and Technology, Doha 24449, Qatar

<sup>3</sup> School of Mechanical and Renewable Engineering, Coventry University, Coventry CV1 5FB, UK

<sup>4</sup> Department of Chemical Engineering, Jordan University of Science and Technology, Irbid 22110, Jordan

\* Correspondence: rajamazuir.shah@udst.edu.qa (R.M.R.A.S.); ac1028@coventry.ac.uk (M.A.Q.)

**Abstract:** Innovations are required for electric vehicles (EVs) to be lighter and more energy efficient due to the range anxiety issue. This article introduces an intelligent control of an organic structure solar supercapacitor (OSSC) for EVs to meet electrical load demands with solar renewable energy. A carbon fibre-reinforced polymer, nano zinc oxide (ZnO), and copper oxide (CuO) fillers have been used in the development of OSSC prototypes. The organic solar cell, electrical circuits, converter, controller, circuit breaker switch, and batteries were all integrated for the modelling of OSSCs. A carbon fibre (CF)-reinforced CuO-doped polymer was utilised to improve the concentration of electrons. The negative electrodes of the CF were strengthened with nano ZnO epoxy to increase the mobility of electrons as an n-type semiconductor (energy band gap 3.2–3.4 eV) and subsequently increased to 3.5 eV by adding 6%  $\pi$ -carbon. The electrodes of the CF were strengthened with epoxy-filled nano-CuO as a p-type semiconductor to facilitate bore/positive charging. They improve the conductivity of the OSSC. The OSSC power storage was controlled by an adaptive neuro-fuzzy intelligent system controller to meet the load demand of EVs and auxiliary battery charging. Moreover, a fully charged OSSC (solar irradiance = 1000 W/m<sup>2</sup>) produced 561 W·h/m<sup>2</sup> to meet the vehicle load demand with 45 A of auxiliary battery charging current. Therefore, the OSSC can save 15% in energy efficiency and contribute to emission control. The integration of an OSSC with an EV battery can minimise the weight and capacity of the battery by 7.5% and 10%, respectively.

**Keywords:** solar organic supercapacitor; ANFIS; electric vehicle; solar energy; renewable energy

**Citation:** Rahman, A.; Myo Aung, K.; Ihsan, S.; Raja Ahsan Shah, R.M.; Al Qubeissi, M.; Aljarrah, M.T. Solar Energy Dependent Supercapacitor System with ANFIS Controller for Auxiliary Load of Electric Vehicles. *Energies* **2023**, *16*, 2690. <https://doi.org/10.3390/en16062690>

Academic Editor: Sheldon Williamson

Received: 5 February 2023

Revised: 22 February 2023

Accepted: 25 February 2023

Published: 13 March 2023



**Copyright:** © 2023 by the authors. Licensee MDPI, Basel, Switzerland. This article is an open access article distributed under the terms and conditions of the Creative Commons Attribution (CC BY) license (<https://creativecommons.org/licenses/by/4.0/>).

## 1. Introduction

Currently, climate change can be regarded as one of the most significant environmental threats. World policymakers have emphasized the commercialisation of EVs in recent years because it has the potential to reduce greenhouse gas emissions, which are mainly produced by internal combustion (IC) engine vehicles. Electricity is a potential clean energy substitute for vehicles in the future that can eliminate the usage of fuel and GHG emissions. One of the biggest setbacks is the lack of fast charging stations for EVs. Electric charging stations are still in the development stages. Moreover, EVs are limited by range and speed. Most EVs have a mileage range of about 50 to 100 and low speed. An EV battery has a longer charging time. While it only takes a couple of minutes to fill up the fuel tank of an IC vehicle, EVs take about 4 to 6 h to get fully charged. Depending on the type and usage, batteries of all EVs must be replaced every 3 to 10 years. In addition, the main traction batteries of EVs are overloaded by car accessories, radios, air conditioning, and the electrical system. These applications drain the batteries more quickly, and charging takes more time. Batteries of EVs are considerably heavy. A battery pack of an

average EV weighs is 450 kg. The heavyweight puts more pressure on batteries and energy drains out faster. Expensive fuel costs and low-carbon awareness are the reasons for alternative solutions such as solar vehicles and EVs [1]. The most important thing for solar vehicles and EVs is the design concept, such as space for solar cells and battery packs [2]. Several studies emphasise hydrogen fuel to achieve the target of net-zero emission. A fuel cell has the highest potential to produce hydrogen energy and convert it to electrical energy [3].

Since the innovation of EVs, numerous studies have sought new technologies to resolve the issues associated with batteries, such as mileage [4], battery life [5] and maintenance cost [6]. One of the promising technologies is the utilisation of organic structural solar supercapacitors (OSSC) as body panels in EVs. Conventional supercapacitor applications have been utilised in EVs, such as energy harvesting via braking and power supply for start–stop systems. The conventional supercapacitor has two disadvantages compared to the regular battery, namely, high energy cost and low specific energy. These issues can be potentially resolved by implementing an OSSC as the body panel of an EV, which improves the energy density and faster discharge time. Supercapacitor applications and solar applications have great potential for advanced improvements. The combination of current activated carbon-based supercapacitors and lightweight solar panels would find its place in commercialisation in the near future as the structural body of an EV. Moreover, a hybrid system that harvested both electrical and solar energy is more efficient and a new trend in green energy [7]. Solar energy is becoming more reliable and predictable with a recent hybrid methodology, namely, “Six Days Ahead Forecasting” [8].

EV range could potentially be improved by integrating organic composite body panels that consist of high-conductive metal oxides, such as copper oxide, graphene oxide, and zinc oxide. Manganese-based oxides are efficient materials to produce electrodes of storage devices due to various crystal structures, higher specific capacitance, and large potential range [9]. Epoxy resin plays an important role in clean energy technology due to its lightweight. It can function as an energy storage device (battery or capacitor), storing energy from various renewable sources. Moreover, it has several benefits, such as 1) being lightweight, 2) storing and supplying on-demand energy, and 3) providing external heat insulators for the vehicle body. Studies showed that by implementing this technology, the energy storage size can be reduced significantly [10].

Nowadays, numerous automobile companies have focused on providing renewable solutions by replacing conventional vehicles with hybrid and electric vehicles. EV brands, such as Tesla, are growing rapidly in terms of market share [11]. EVs are better than an internal combustion vehicle in terms of operational cost, advanced features, and carbon emission [12]. To dominate the automobile market in the future, EVs should be improved in terms of range and charging infrastructure [13]. The improvement should start from the design phases to overcome the limitations of EVs via the type of application, desired performance, duty cycles analysis, vehicle parameterisation studies, and a deep understanding of vehicle use purposes [14]. Moreover, Liu et al. [15] presented the effect of low-carbon awareness and government subsidy on EV manufacturers. The next crucial method is the implementation of an energy management system (EMS) that controls the efficiency of EVs [16,17].

Due to their high-power density, fast charging time, and longer cycle life, supercapacitors have advantages over conventional batteries and fuel cells [18,19]. Carbon is the most commonly used material for the fabrication of supercapacitor electrodes because it has various properties such as low cost, high conductivity, high-temperature stability, environmental friendliness, and high surface area. Graphenes, carbon fibres, carbon aerogels, activated carbon, and carbon nanotubes are the most utilised forms of carbon for the fabrication of supercapacitor electrodes [20]. Carbon fibre has abundant pores at the surface, which contributes to the high absorption of ions. Moreover, the one-dimensionality of CF provides superior charge transport properties. These significant properties are the underlying parameters for carbon fibre as common electrode material for electric double-layer capacitors [21,22].

This paper presents the modelling and development of solar supercapacitors as body panels of EVs. The OSSC serves both as a photovoltaic energy generator and renewable energy storing device by solar heat trapping. The system can provide precise power to an EV's auxiliary battery and load. By utilising the experimental data of OSSC samples that are made up of CuO/ZnO and epoxy resin sandwiched between carbon fibre sheets, the OSSC system was modelled in Simulink. The efficiency of the OSSC and power management system (PMS) were investigated via ANFIS simulation.

## 2. Development Methodology of AI OSSC

### 2.1. Development of the OSSC System

An OSSC utilised as a vehicle body panel can also act as an insulator. A higher electron transfer was achieved by copper oxide powder. High catalytic activity and a larger surface area of zinc oxide contribute to an efficient catalytic reaction process [23]. A faster charging time was achieved by synthesising CuO with ZnO. Epoxy resin as a conducting polymer prevented quick discharging as in conventional capacitors. Solar energy was converted to electrical and thermal energy by devices known as photovoltaic thermal hybrid solar collectors. A system with a solar thermal collector and solar cells can improve efficiency by removing the waste heat from the PV module and capturing the remaining energy. Hence, a stand-alone system was less energy-efficient than a hybrid system. The OSSC panel with the presence of conducting polymer converted the solar energy to electricity and stored it.

The organic solar cell, electrical circuits, converter, controller, circuit breaker switch, and batteries were all integrated for the modelling of an OSSC. The OSSC was developed by utilising zinc oxide (ZnO), copper oxide (CuO), ER, CF, and a separator/ $\text{Na}_2\text{SO}_4$  electrolyte, as shown in Figure 1. CF-reinforced CuO-doped polymer was utilised to increase electron concentration.

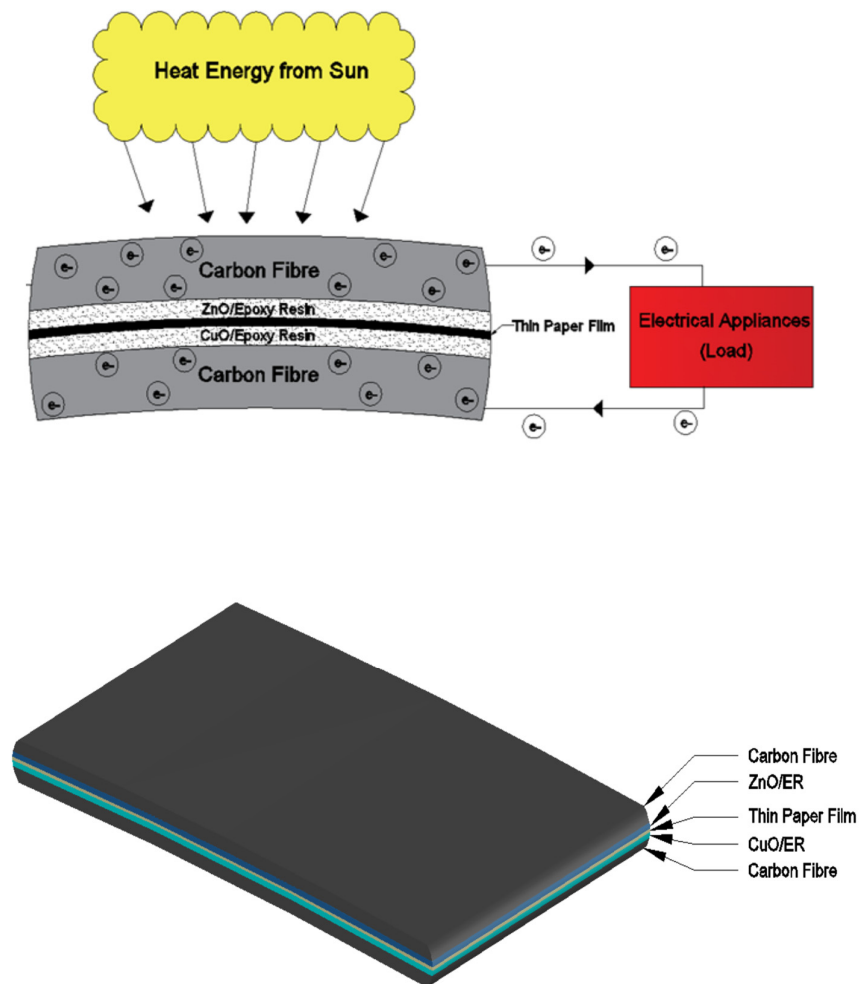
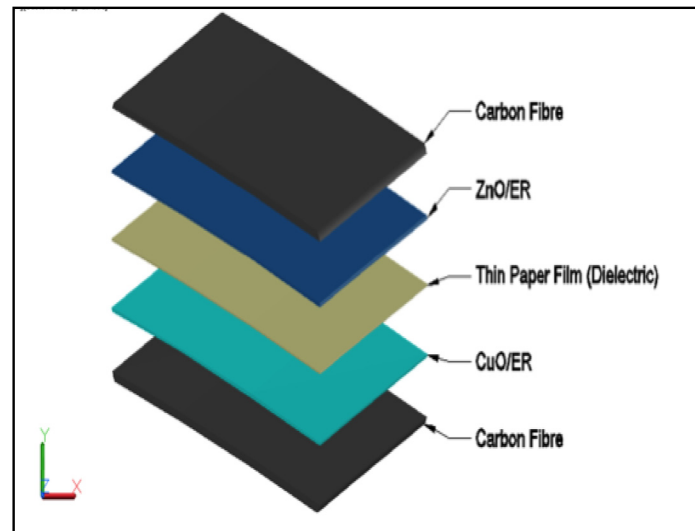


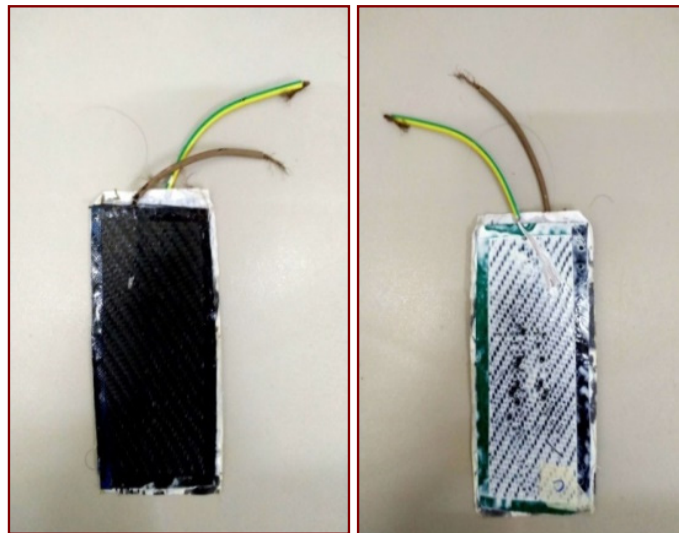
**Figure 1.** Operating concept of OSSC.

### 2.1.1.1. Development Process of the OSSC

CF fabrics derived from PiCarbon ( $240 \text{ g/m}^2$ ) that were  $0.25 \text{ mm}$  thick were selected for the development of the OSSC. CF acts as a rising electrode. Based on the compatibility with CF, the ER and hardener were selected. The transparent ER and hardener have a recommended mixing ratio of 2:1 and a full 24 h curing period between  $25 \text{ }^\circ\text{C}$  and  $30 \text{ }^\circ\text{C}$ . Nano ZnO epoxy was added to the CF electrodes and became the negative electrode. The negative electrode had a bandgap energy of  $3.2 \text{ eV}$  to  $3.4 \text{ eV}$  as an n-type semiconductor. By adding  $6\% \pi$ -carbon, the bandgap energy increased to  $3.5 \text{ eV}$ . The CF electrodes were reinforced with epoxy-filled nano-CuO as a p-type semiconductor to facilitate bore/positive charging. They improved the conductivity of the OSSC. The dielectric separator film was placed between the ZnO-doped ER and the CuO-doped ER. A laboratory-scale sample of the solar supercapacitor is shown in Figure 2.



(a)



(b)

**Figure 2.** Sample of solar supercapacitor (a) exploded view and (b) prototype units.

### 2.1.2. PV Cells

The PV effect is a physical and chemical phenomenon that converts solar energy to electricity. A PV cell generates electricity through the photovoltaic effect. The electrical characteristics of PV cells, such as the current, voltage, and resistance, vary when exposed to light. PV modules, also known as PV panels, are made up of blocks of PV cells. PV panels are one of the best technologies for solar energy harvesting. The cost per watt, solar energy conversion efficiency, and practicality determine the various applications of PV cells [24]. Comparing the two types of PV cells available in this time and era gives a clear picture of their suitability for different application scenarios. The differences between organic PV cells and inorganic PV cells according to [25,26] are summarised and presented in Table 1.

**Table 1.** Difference between organic and inorganic PV cells.

Attributes	Organic PV	Inorganic PV
Life cycle	10,000 h	10 years
Efficiency	~10%	~25%
Cost impact	low	high
Transparency	transparent	opaque
Integration	easy	difficult
Flexibility	flexible	solid
Weight	very light	heavy

## 2.2. ANFIS PV OSSC

Artificial Intelligence (AI) is a process to simulate human intelligence by computer systems that can analyse large-scale data. There are three types of AI techniques, namely, fuzzy logic (FL), adaptive network-based fuzzy inference systems (ANFISs), and artificial neural networks (ANNs) [27]. There are two major types of training techniques for AI, namely, unsupervised training and supervised training. Without any external feedback, unsupervised models train the input data by learning the pattern, while supervised training requires a set of input data and predefined output data [28]. Takagi–Sugeno fuzzy inference system is the foundation of ANFISs. It has the potential benefit of combining neural networks and fuzzy logic principles. Nonlinear functions can be estimated by a set of fuzzy ‘If-Then’ rules [29]. The gradient method calculates the input membership function parameters, and the least square method calculated the parameters of the output function. Using the first-order Sugeno model and two fuzzy ‘IF-Then’ rules, the ANFIS configuration can be represented by the following rules and equations:

Rule (1): IF  $x$  is  $a_1$  AND  $y$  is  $b_1$ , THEN

$$f_1 = p_1x + q_1y + r_1 \quad (1)$$

Rule (2): IF  $x$  is  $A_2$  AND  $y$  is  $B_2$ , THEN

$$f_2 = p_2x + q_2y + r_2 \quad (2)$$

where

$f_i$  = fuzzy rule output;

$x_i$  and  $y_i$  = fuzzy rule inputs;

$a_i$  and  $b_i$  = fuzzy sets;

$p_i$ ,  $q_i$ , and  $r_i$  = parameters of design defined at the training process.

The configuration of the ANFIS was fixed with many parameters, which caused a tendency for the system to overfit trained data, particularly with a big number of training epochs. A trained ANFIS potentially cannot adapt effectively to other independent data sets if overfitting occurs. For an ideal situation, the efficiency of the converters was considered 0.9. The mathematical model of solar power ( $P_{\text{solar}}$ ) is represented in Equation (3).

$$P_{\text{solar}} = (V_{\text{max}} N_s) (I_{\text{max}} N_p) \quad (3)$$

where

$V_{\text{max}}$  = maximum voltage;

$N_s$  = number of solar modules in series;

$I_{\text{max}}$  = maximum current;

$N_p$  = number of solar modules in parallel.

The mathematical models of battery power ( $P_{\text{batt}}$ ) and supercapacitor power ( $P_{\text{sc}}$ ) are determined by Equations (4) and (5), respectively.

$$P_{\text{batt}} = I_{\text{batt}} V_{\text{batt}} \quad (4)$$

$$P_{\text{sc}} = I_{\text{sc}} V_{\text{sc}} \quad (5)$$

where

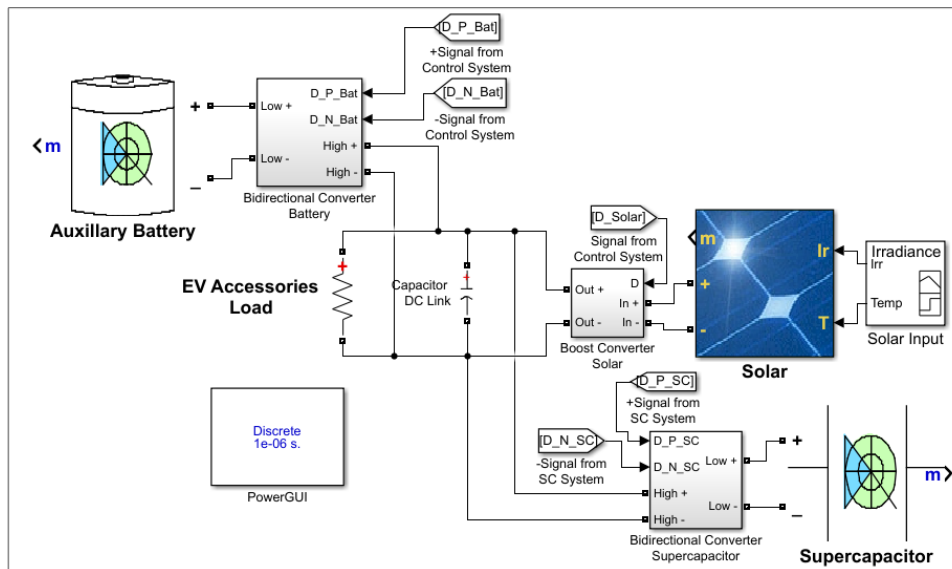
$I_{batt}$  = battery current;

$V_{batt}$  = battery voltage;

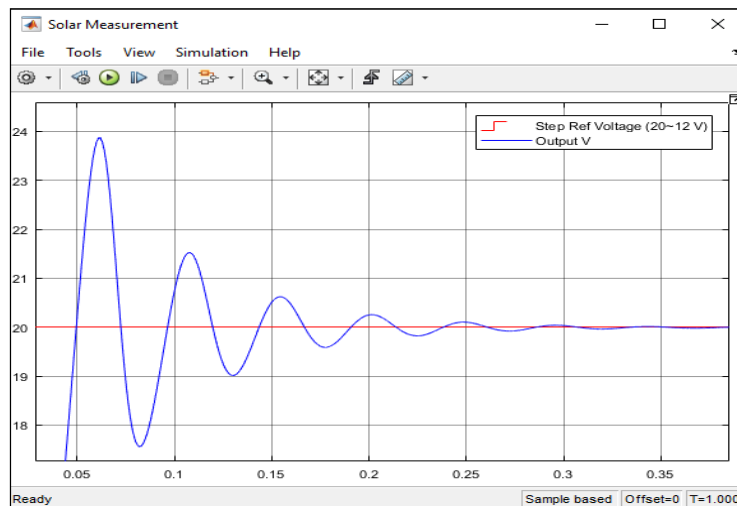
$I_{sc}$  = supercapacitor current;

$V_{sc}$  = supercapacitor current voltage.

The power simulation was conducted using the Simulink model as shown in Figure 3. The power consumption of EV loads, such as starting, lighting system, instrumentation system, dashboard, wiper motor, power windows motor, and air-conditioning power, was simulated with the product of the load voltage and load current from the load sensors. The supply and charging powers of the supercapacitor were simulated with the product of the supercapacitor voltage and supercapacitor current from the sensors.  $P_{solar}$  was simulated with the product of the solar panel voltage and solar panel current. To test the efficiency of the solar supercapacitor in the real-life cycle, the input irradiance was set as variable irradiance in the range of 200–2000 W/m<sup>2</sup>.



(a)



(b)

**Figure 3.** ANFIS model (a) system architecture and (b) output voltage profile of solar panel without controller at 1000 W/m<sup>2</sup>.

Table 2 demonstrates the simulation results from the Simulink model of the OSSC panel based on two input parameters, namely, a constant temperature of 25 °C and a solar input irradiance in the range of 200–1000 W/m<sup>2</sup>. The ANFIS rules and the structure of membership functions (input and output) are shown in Figure 4. The simulation results of P<sub>solar</sub> from Table 2 were employed in the ANFIS training data, as shown in Figure 5.

**Table 2.** P<sub>solar</sub> simulation results (OSSC size of 9.75 m<sup>2</sup>).

Input Parameter		Output
Temperature (°C)	Irradiance (W/m <sup>2</sup> )	P <sub>solar</sub> (W)
25	1000	957.1
25	800	729.1
25	600	584.1
25	400	388.4
25	200	180.8

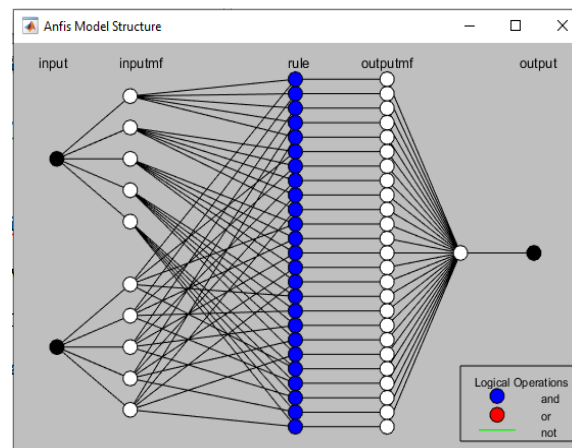


**Figure 4.** ANFIS network structure for P<sub>solar</sub>.

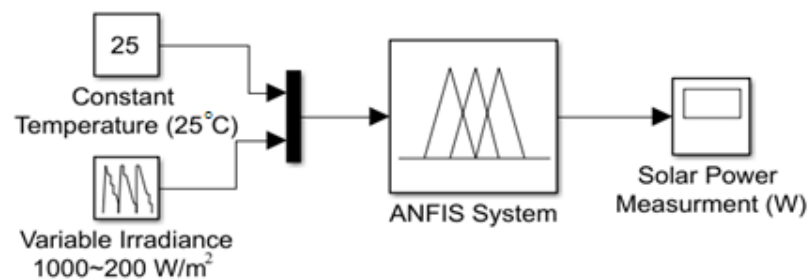


**Figure 5.** P<sub>solar</sub> ANFIS model.

In terms of P<sub>batt</sub>, two inputs were used, namely, irradiance and load. Irradiance input has 5 membership functions (constant 1000 W/m<sup>2</sup>), and the load input has 5 membership functions based on the load of the EV’s electrical system (500~100 W). The ANFIS rules and the structure of the membership functions (input and output) are shown in Figure 6. The results of the P<sub>batt</sub> simulation from Table 3 were used in the ANFIS training data as shown in Figure 7. The solar irradiance was put as a constant input profile with the value of 1000 W/m<sup>2</sup> and EV’ load was set as a variable load profile between 100 W and 500 W.

**Table 3.**  $P_{batt}$  simulation results.

Input Parameters		Output
Irradiance ( $W/m^2$ )	Load (W)	$P_{batt}$ (W)
1000	500	-375.6
1000	400	-453.4
1000	300	-525.4
1000	200	-610.8
1000	100	-705.3

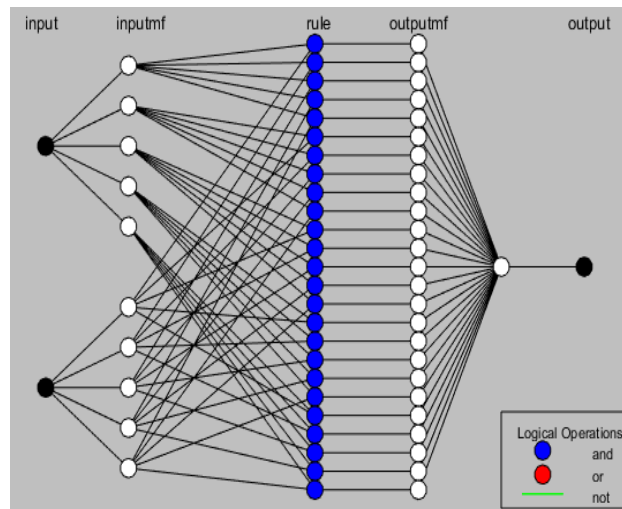


**Figure 6.** ANFIS network structure for  $P_{batt}$ .

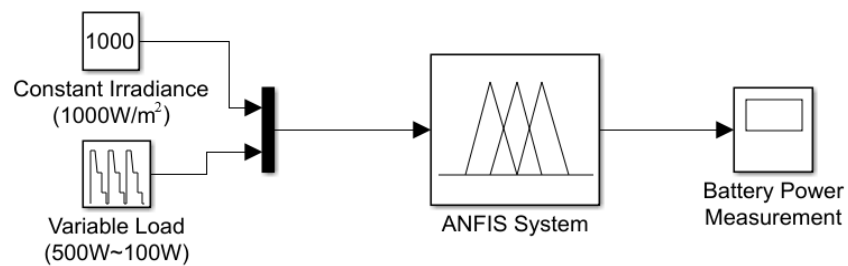


**Figure 7.**  $P_{batt}$  ANFIS model.

The ANFIS model was working more efficiently to provide accurate results with varying input values. Moreover, the ANFIS model has provided efficient solar output values by training the input data of the fuzzy interference system. At  $1000 W/m^2$  solar irradiance, the system generated the highest solar output of  $560 W$ , as shown in Figure 8.

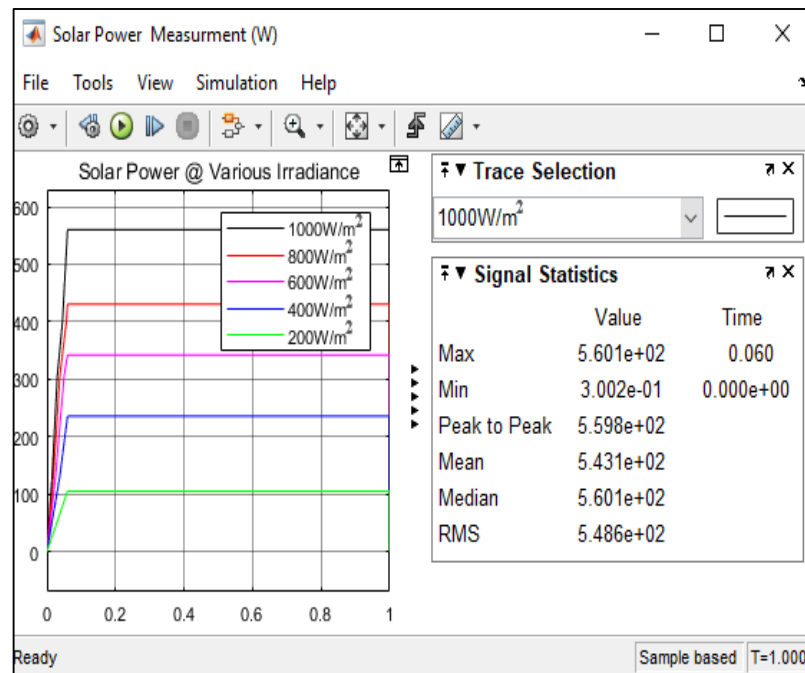


**Figure 8.**  $P_{\text{solar}}$  at different irradiance settings by ANFIS model.

For practical utilisation, the input irradiance changes with respect to the geographical location of the device. The profile of solar irradiance was defined in four conditions at total daytime (TDT), namely, (1) 1000 W/m<sup>2</sup> at 30% TDT, (2) 500 W/m<sup>2</sup> at 30% TDT, (3) 200 W/m<sup>2</sup> at 30% TDT, and (4) 0 W/m<sup>2</sup> at 10% TDT. Using signal statistics from the Simulink model, the mean  $P_{\text{solar}}$ /specific period was 495.4 W.

Equation (6) determines the potential performance of a solar supercapacitor:

$$P_{\text{sys}} = P_{\text{sol}} + P_{\text{batt}} + P_{\text{sc}} \quad (6)$$

The average size battery capacity of an EV is 50 kW·h. For instance, Tesla Model 3 with a similar battery capacity can achieve a 400 km range on a standard duty cycle. Based on Equation (6), an energy of 2.3 kW·h can be obtained from a fully charged solar capacitor (1000 W/m<sup>2</sup>) or a 4.56% increase compared to the conventional EV range.

The performance of the solar supercapacitor, fuzzy controllers, and overall efficiency of the system were investigated. The precise power distribution among various storage systems was achieved by the PMS of the OSSC. The power requirements of the EV accessories load were supported by the power generation of the proposed OSSC. The OSSC output was able to decrease the size of the EV battery and weight by 10% and 7.5%, respectively. In addition, the integration of EVs and OSSCs could contribute to the reduction of manufacturing costs by 10% due to the reduced battery size. Subsequently, it reduces greenhouse gas emissions by 25% based on IC engine vehicle greenhouse gas emissions data at 2.31 kg-CO<sub>2</sub>/litre.

### 2.3. Variable Load and Variable Irradiance

The performance of the OSSC PMS was studied at different irradiance levels and different EV electrical load demands, as shown in Figures 9 and 10. At 1000 W/m<sup>2</sup> at a solar temperature of 25 °C, the solar supercapacitor system of size of 2 m<sup>2</sup> produced  $P_{\text{solar}} = 1122$  W and charged the EV batteries at 88 A. For 500 W/m<sup>2</sup> at a solar temperature of 25 °C, the OSSC generated  $P_{\text{solar}} = 885$  W and charged the EV batteries at 70 A, which was low for EV battery charging power. It can be concluded that the OSSC alone was not enough to charge the EV batteries. Hence, an auxiliary battery was used to supply 5 A to the OSSC to speed up the charging current for the EV's batteries.

A total of 200 W/m<sup>2</sup> at a solar temperature of 25 °C can deliver only 35 A, which was significantly low to meet the load demand of 65 A. Thus, the auxiliary battery was required to provide more load to the OSSC at 30 A to meet the EV’s load demand of 65 A. It can be concluded that the organic solar structure capacitor (OSSC) was only effective at a solar temperature of 32 °C and above.

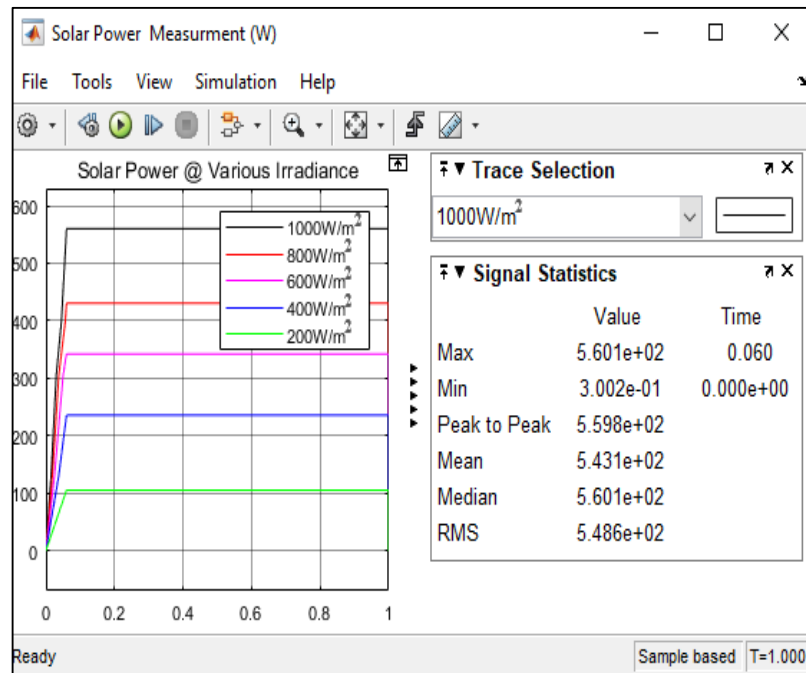


Figure 9. P<sub>solar</sub> at different load settings by ANFIS model.

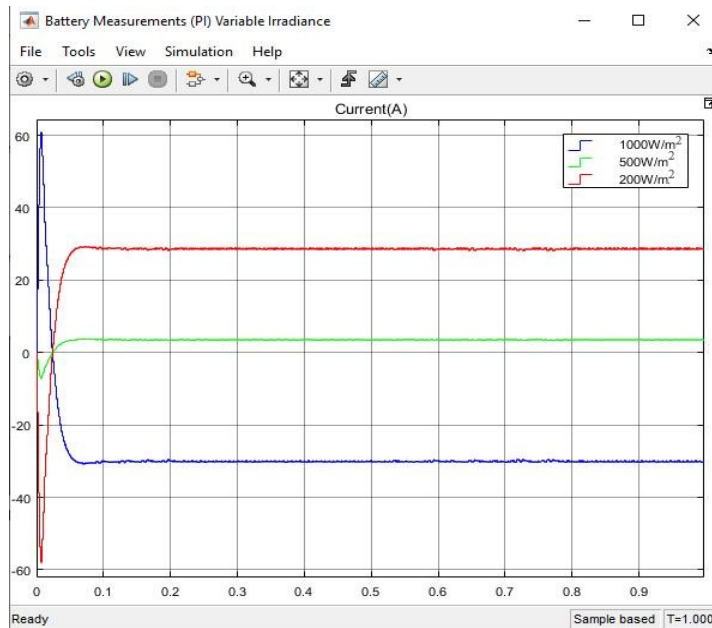


Figure 10. Battery current profile at three irradiance levels.

In terms of power comparison, Table 4 shows the differences between the experimental method, Simulink model, and ANFIS model. The errors were significantly low between the experimental method and the Simulink model, which indicated that the Simulink model

performed almost similar behaviour to the physical system. The error was slightly higher between the experimental method and the ANFIS model but still within the acceptable range.

**Table 4.** Power comparison between experimental results, Simulink model, and ANFIS model.

Irradiance (W/m <sup>2</sup> )	Experimental (i) (W)	Simulink Model (ii) (W)	ANFIS Model (iii) (W)	Errors (%)	
				(i) vs. (ii)	(i) vs. (iii)
1000	959.976	957.1	972.3	0.271	1.296

Table 5 shows the power comparison between the mathematical model, Simulink model, and ANFIS model. For the mathematical model, the efficiency of the converters was set at 93% according to the common value. For the Simulink and ANFIS models, the results were simulated using the actual parameters of the converter components.

The error between the mathematical model and the Simulink model was less than 7%. This was mainly due to the high losses during the current flow to the battery that needed to pass several converters. In practical applications, the efficiency of the converter will decrease with a higher current. Therefore, it was efficient to design the system with a high operating voltage and low operating current.

**Table 5.** Power comparison between mathematical model, simulation model, and ANFIS model.

	Mathematical Model (i) (W)	Simulink Model (ii) (W)	ANFIS Model (iii) (W)	Errors (%)	
				(i) vs. (ii)	(i) vs. (iii)
		Irradiance (W/m <sup>2</sup> )			
1000	976	957.1	972.3		
600	584	584.5	594.1	5.83%	1.72%
200	192	180.8	182.6		
		Load (W)			
500	-397.17	-375.6	-377.1		
300	-564.03	-525.4	-532.6	6.85%	1.35%
100	-730.85	-705.3	-703.4		

#### 2.4. OSSC with PI Controller

The solar supercapacitor system design must be able to charge and discharge. Therefore, the performance of bidirectional converters with PI controllers was investigated at a constant irradiance of 1000 W/m<sup>2</sup> (optimal condition). The PI controller parameters are shown in Table 6. The model architecture of the PI controller for the OSSC is shown in Figure 11. The voltage and power were supplied to the load at 12.4 V and 524 W, respectively.

**Table 6.** Parameters of bidirectional controllers.

PI Controller	Transfer Function
Solar reference	$K_p = 1.45, K_i = 3099$
Battery signal	$K_p = 4.5, K_i = 60$
Supercapacitor signal	$K_p = 0.5, K_i = 15,000$
Switching frequency	15 kHz

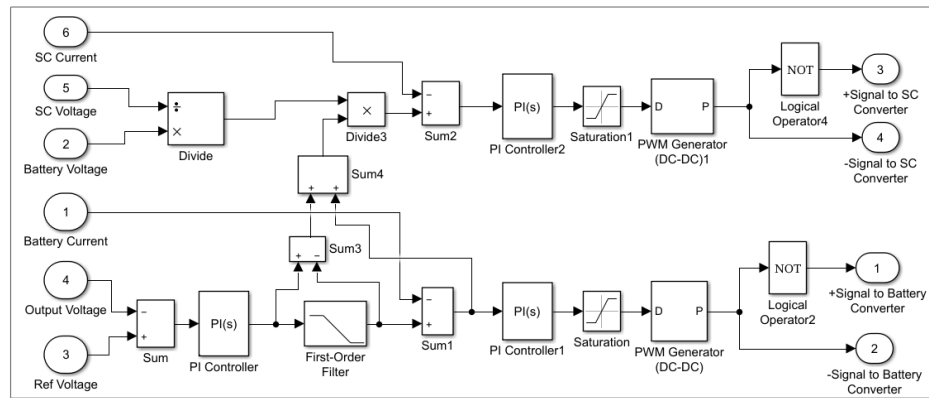
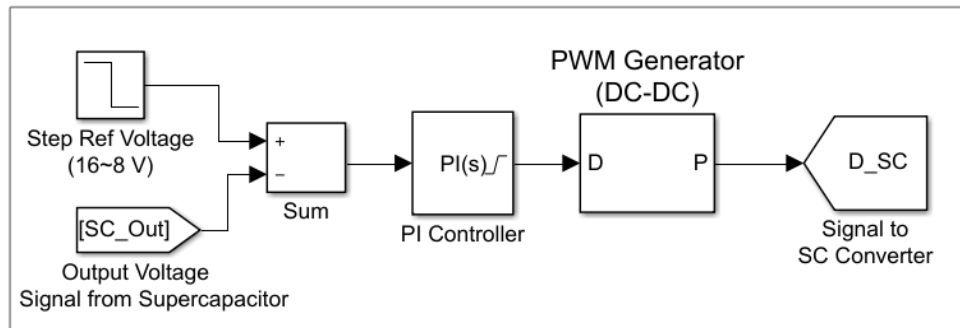
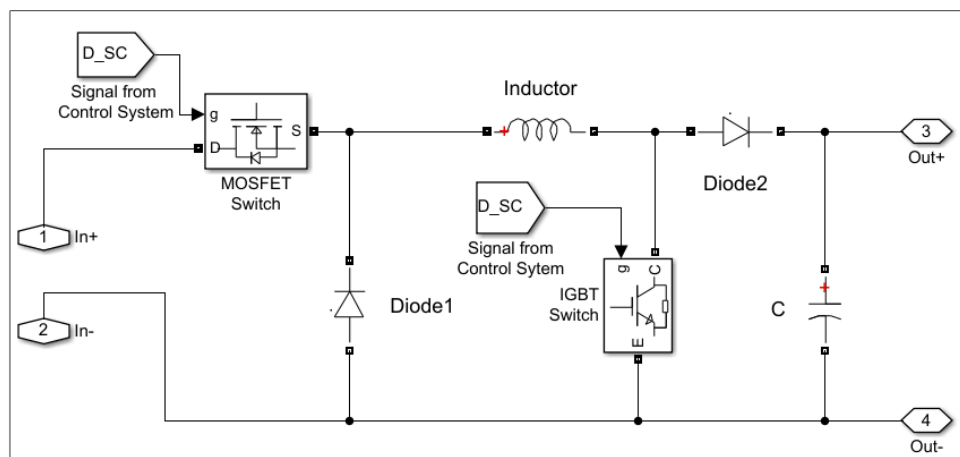


Figure 11. Control system with PI controllers for battery and supercapacitor.

The PI converter control system of the OSSC model is shown in Figure 12. The reference voltage range was set as 8~16 V, and the difference between the reference voltage and battery voltage was used as an error signal to the PI controller, as shown in Figure 12a. The output from the PI controller was switched to a pulse width modulation (PWM) signal and sent to control switches, as shown in Figure 12b.



(a)

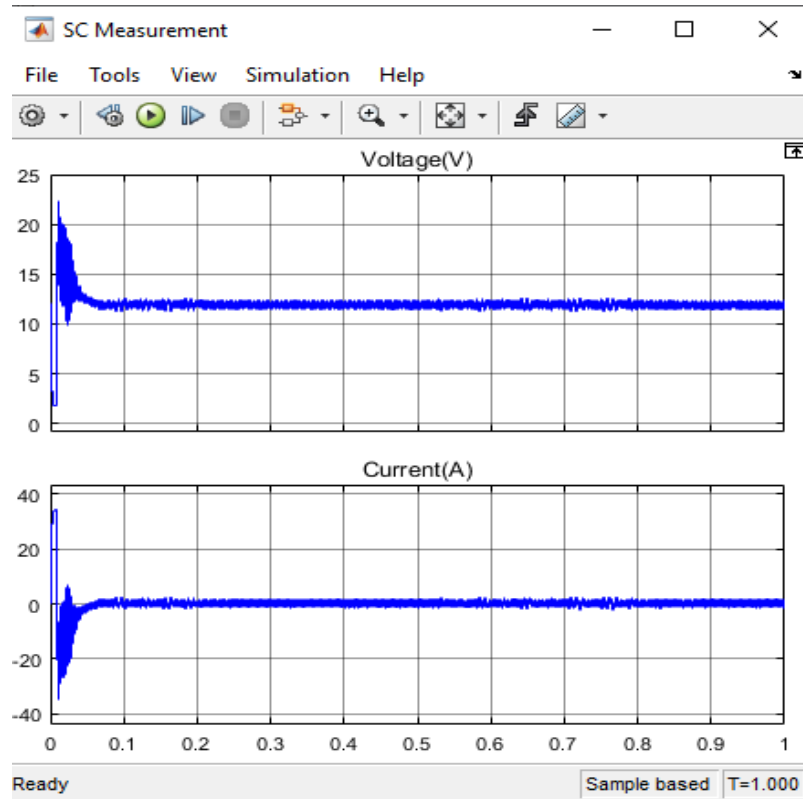


(b)

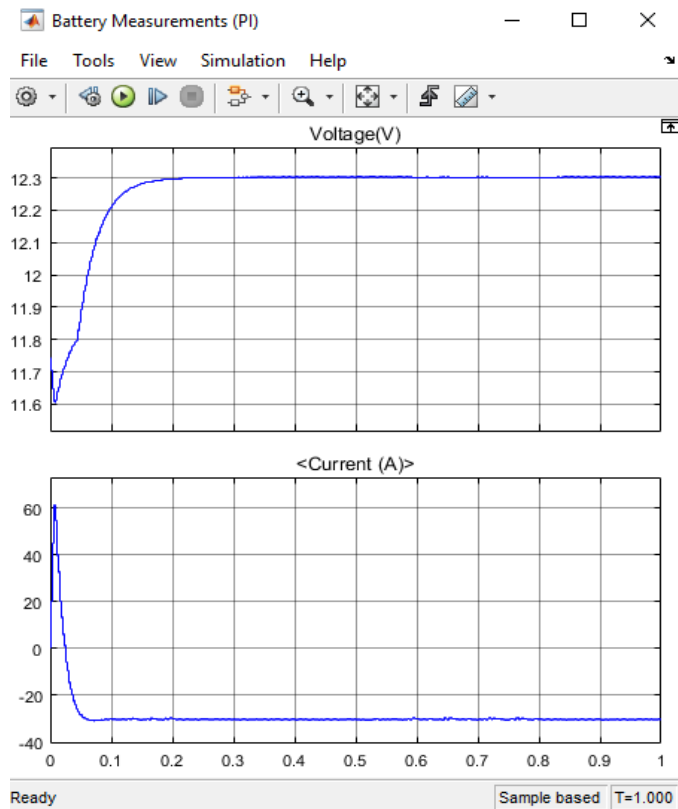
Figure 12. One-directional PI power management system for supercapacitor (a) control system and (b) converter system.

The voltage and current supplied by the OSSC panel of size 1 m<sup>2</sup> at irradiance 1000 W/m<sup>2</sup> are shown in Figure 13a. The voltage and current of the solar panel reached the maximum

value at 23 V and 38 A, respectively, within 0.03 s. This was due to the maximum power point tracking system being operated efficiently. Both parameters stabilised at 0.06 s with a value of 13 V and 7 A. On the other hand, the auxiliary battery discharged current reduced sharply within 0.05 s when solar irradiance was introduced as shown in Figure 13b.



(a)



(b)

Figure 13. Voltage and current profiles for (a) supercapacitor and (b) auxiliary battery profile.

2.5. OSSC with FL Controller

FL uses natural values to perform computer processes rather than binary values. FL relies on the levels of state of input and output as a function of the rate change at this state. FL assigns a specific output based on the probability of the input’s state. FL also works on the principle of determining the output depending based on knowledge-based data. The variables for a multi-input system are different inputs, and the output is the potential result of the ‘AND’ operation among the variables. Based on these principles, the OSSC with the FL controller (FLC) was developed in Simulink as shown in Figure 14.

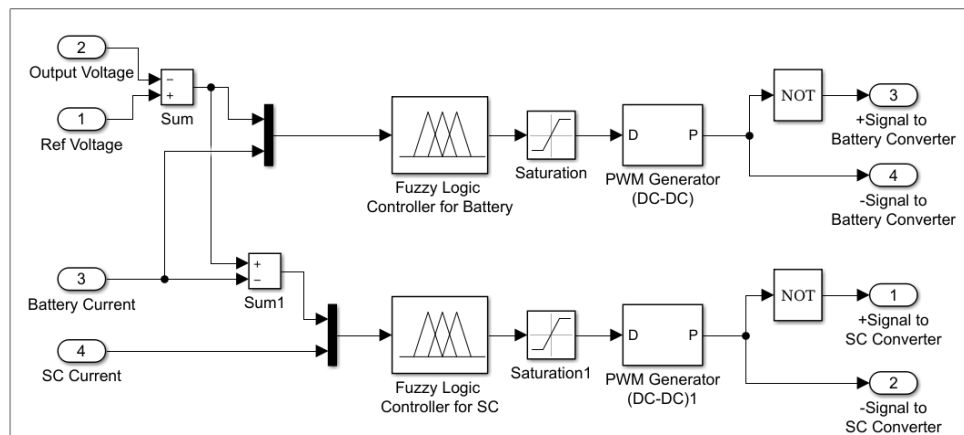


Figure 14. Control system with FLC for battery and supercapacitor.

The PMS of the OSSC was designed to be managed by an FLC. The difference between the output voltage and reference voltage was used as an error signal. The error signal and battery current were set as input signals for the FLC. The FLC produced duty cycle signals which were converted to PWM signals and sent to converter systems as opposite signals. The FLC signals determined the amount of current to the load and the mode of the storage devices. The difference between the error signal from the battery and the battery current was sent as an error signal for the supercapacitor control system. The error signal and supercapacitor current were set as input signals for the FLC of the supercapacitor.

Figures 15 and 16 show the maximum power point tracking (MPPT) control system and converter system of the solar panel for both the PI and FLC. The MPPT of the solar panel was achieved by the P and O method, which increases or decreases the duty cycle until maximum voltage and current were achieved. The parameters of PMS are shown in Table 7.

**Table 7.** Parameters of solar PMS.

Switching Frequency	Values (at 5 kHz)
Converter inductance	0.352 mH
Converter capacitance	2200 $\mu$ F
Converter resistance	50 mOhm
Diode resistance	0.1 mOhm
IGBT resistance	1 mOhm

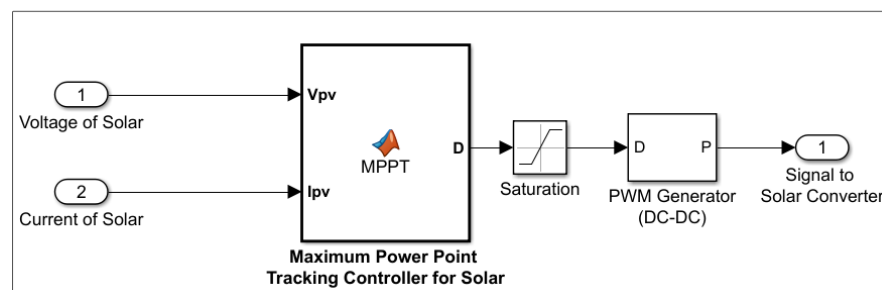


**Figure 15.** MPPT solar control system.

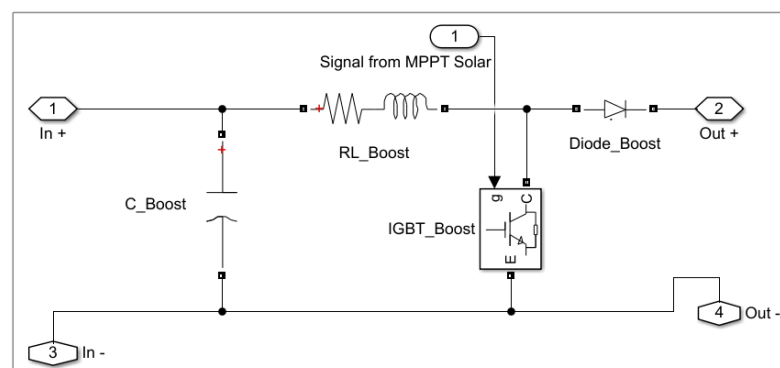


**Figure 16.** DC-DC solar converter system of MPPT using the P and O method.

‘Ref Current’ (error signal) and ‘Battery Current’ were the inputs of the FLC, and ‘Duty Cycle’ was the output of the FLC, as shown in Figure 17. The membership functions of ‘Ref Current’ were set as ‘Very Low (VL)’ (–15 to –7.5), ‘Low (L)’ (–15 to 0), ‘Zero (Z)’ (–7.5 to 7.5), ‘High (H)’ (0 to 15), and ‘Very High (VH)’ (7.5 to 0), as shown in Figure 17a. The membership functions of ‘Battery Current’ were set as ‘High Charging (HC)’ (–30 to –15), ‘Low Charging (LC)’ (–30 to 0), ‘Zero (Z)’ (–15 to 15), ‘Low Discharging (LD)’ (0 to 30), and ‘High Discharging (HD)’ (15 to 30), as shown in Figure 17b. The membership functions of ‘Duty Cycle’ were set

as ‘Negative Big (NB)’ (−1 to −0.5), ‘Negative Small (NS)’ (−1 to 0), ‘Zero’ (−0.5 to 0.5), ‘Positive Small (PS)’ (0 to 1), and ‘Positive Big (PB)’ (0.5 to 1), as shown in Figure 17c.

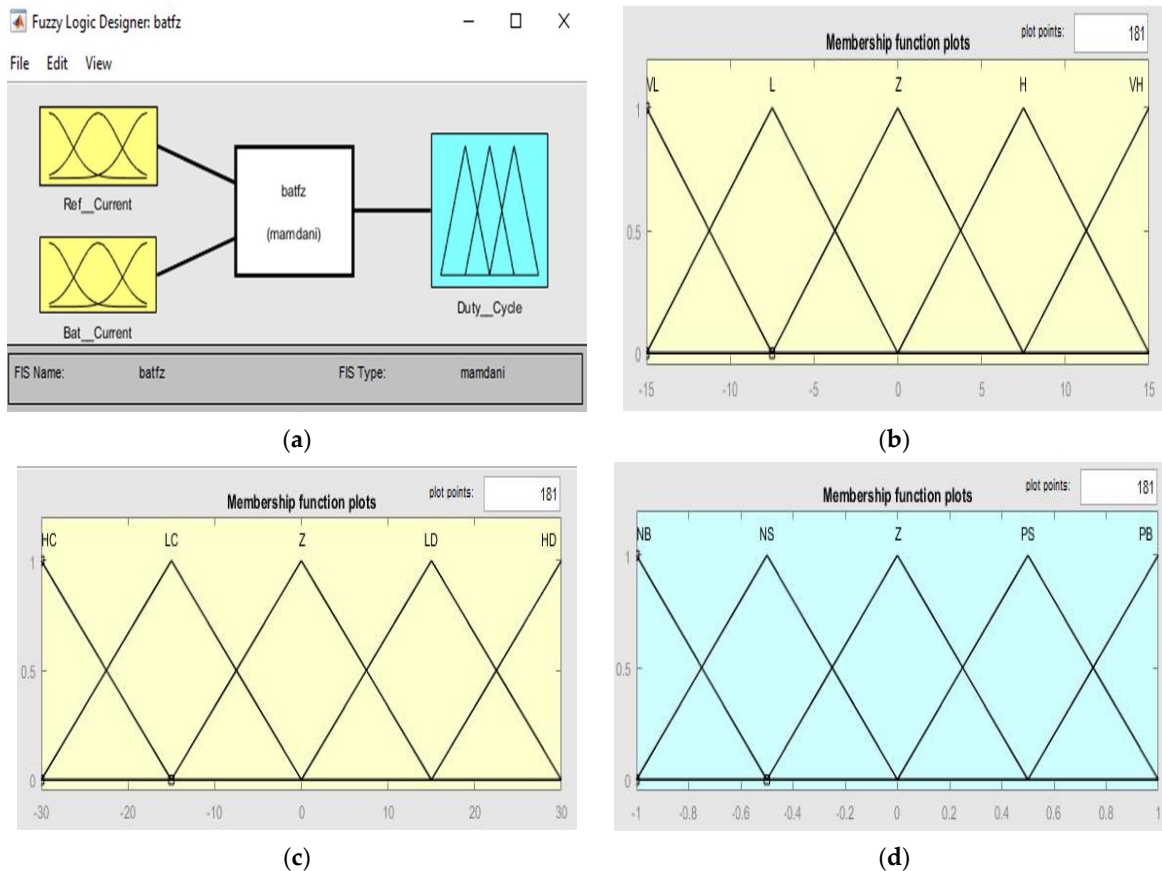


**Figure 17.** FLC of auxiliary battery. (a) Fuzzy inference system for OSSC; (b) reference current; (c) battery current; and (d) duty cycle.

‘Error Ref’ (error signal) and ‘Supercapacitor Current’ were the inputs of the FLC, and ‘Duty Cycle’ was the output of the FLC. The membership functions of inputs of the SC FLC were set based on Figure 18a. The membership functions of ‘Error Ref’ were set as ‘Very Low’ (−15 to −7.5), ‘Low’ (−15 to 0), ‘Zero’ (−7.5 to 7.5), ‘High’ (0 to 15), and ‘Very High’ (7.5 to 0), as shown in Figure 18b. The membership functions of ‘Supercapacitor Current’ were set as ‘High Charging’ (−30 to −15), ‘Low Charging’ (−30 to 0), ‘Zero’ (−15 to 15), ‘Low Discharging’ (0 to 30), and ‘High Discharging’ (15 to 30), as shown in Figure 18c. The membership functions of ‘Duty Cycle’ were set as ‘Negative Big’ (−1 to −0.5), ‘Negative Small’ (−1 to 0), ‘Zero’ (−0.5 to 0.5), ‘Positive Small (PS)’ (0 to 1), and ‘Positive Big (PB)’ (0.5 to 1), as shown in Figure 18d. Fuzzy rules for the battery and supercapacitor are shown in Tables 8 and 9.

**Table 8.** Fuzzy rules (R) for battery.

		Battery_Current				
		HC	LC	Z	LD	HD
Ref_current	VH	(-0.5~0.5) R:1	(0~1) R:2	(0~1) R:3	(0.5~1) R:4	(0.5~1) R:5
	H	(-1~0) R:6	(-0.5~0.5) R:7	(0~1) R:8	(0~1) R:9	(0.5~1) R:10
	Z	(-1~0) R:11	(-1~0) R:12	(-0.5~0.5) R:13	(0~1) R:14	(0~1) R:15
	L	(-1~-0.5) R:16	(-1~0) R:17	(-1~0) R:18	(-0.5~0.5) R:19	(0~1) R:20
	VL	(-1~-0.5) R:21	(-1~-0.5) R:22	(-1~0) R:23	(-1~0) R:24	(-0.5~0.5) R:25

**Table 9.** Fuzzy rules (R) for supercapacitor.

		Rate of Error ( $\Delta e$ )				
		HC	LC	Z	LD	HD
Error (e)	VH	(-0.5~0.5) R:1	(0~1) R:2	(0~1) R:3	(0.5~1) R:4	(0.5~1) R:5
	H	(-1~0) R:6	(-0.5~0.5) R:7	(0~1) R:8	(0~1) R:9	(0.5~1) R:10
	Z	(-1~0) R:11	(-1~0) R:12	(-0.5~0.5) R:13	(0~1) R:14	(0~1) R:15
	L	(-1~-0.5) R:16	(-1~0) R:17	(-1~0) R:18	(-0.5~0.5) R:19	(0~1) R:20
	VL	(-1~-0.5) R:21	(-1~-0.5) R:22	(-1~0) R:23	(-1~0) R:24	(-0.5~0.5) R:25

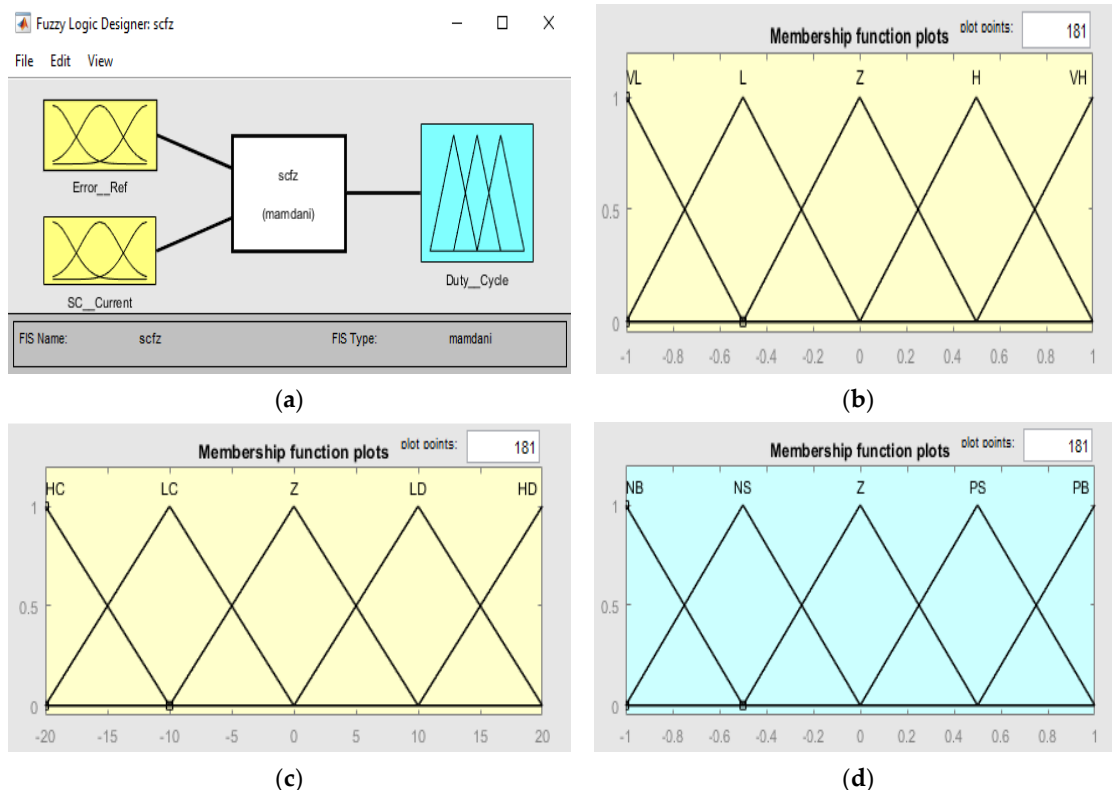


**Figure 18.** FLC of OSSC. (a) Fuzzy inference system for OSSC; (b) reference current; (c) OSSC current; and (d) duty cycle.

The performance of the bidirectional converter with the FLC was tested at a constant irradiance of  $1000 \text{ W/m}^2$  (optimal condition). The voltage and current profile of the OSSC are shown in Figures 19 and 20. On the other hand, the performance of the solar supercapacitor PMS with the FLC was tested at different irradiance settings and different load conditions. The battery charged with a 30 A current while supporting the EV's load (500 W) via the solar supercapacitor system at an input irradiance value of  $1000 \text{ W/m}^2$ . With an input irradiance value of  $500 \text{ W/m}^2$ , the EV load cannot be fully supported by solar power alone. Hence, the EV load was partially supported by the auxiliary battery with a 4 A current. With a low irradiance value of  $200 \text{ W/m}^2$ , the EV load required 28 A current from the auxiliary battery. The battery was charging with an 8 A current when the load value was set as 800 W. When the load value decreased to 300 W, the battery charged with a 48 A current. With a low load value of 100 W, the battery charged with a 70 A current generated by the solar supercapacitor system. The PMS with the FLC was operating more efficiently to provide accurate signals to the converter system.

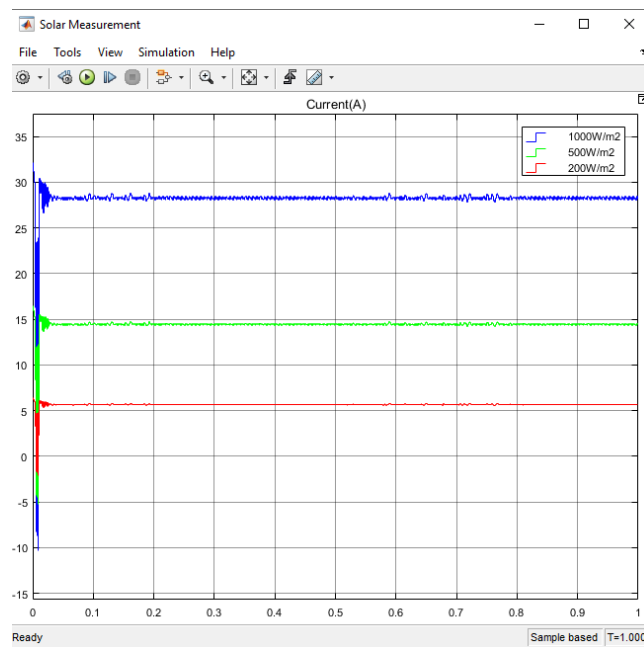


Figure 19. OSSC performance using FLC.

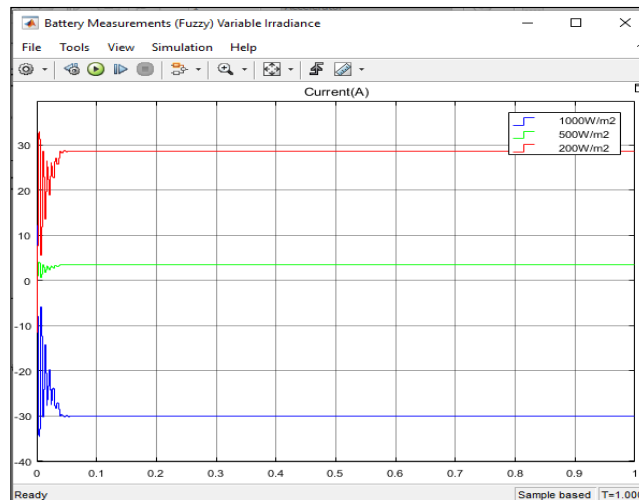


Figure 20. Current profile of battery at different load settings.

Table 10 shows the performance of the ANFIS compared to the FLC and PID based on the simulation performance. The comparison was made with the OSSC 12.5 V output voltage control by simply following the voltage of battery terminals and avoiding high voltage damage to the battery. The performance of the ANFIS in the current generation from the OSSC at irradiance = 1000 W/m<sup>2</sup> was 16% higher than PID and 29% higher than the FLC. In overshooting time, the current stabilisation performance for charging the auxiliary battery was 133% higher than the PID and 0% higher than the FLC. The results indicated that the ANFIS can provide better performance to meet vehicle load demand and control battery charging performance with 0% error.

**Table 10.** ANFIS best for OSSC PMS at irradiance = 1000 W/m<sup>2</sup>.

	OSSC	ANFIS	PID	FLC	% of ANFIS Over	
					PID	FLC
Current	Maximum (A)	45	38	32	16	29
	Stabilised (A)	45	10	27	77	40
	Overshoot (ms)	0.03	0.07	0.03	133	0

A similar conclusion could be made between the ANFIS and FLC based on Table 11. The ANFIS performance was better than the FLC's in terms of the output power generation to meet the vehicle load demand for irradiance range = 200–1000 W/m<sup>2</sup>. These results showed that the ANFIS with the OSSC was reliable and efficient to control the power flow to meet the load demand and auxiliary battery charging.

**Table 11.** Solar power output (ANFIS vs. FLC) at 12.5 V of EV's electrical system.

Temperature (°C)	Irradiance (W/m <sup>2</sup> )	Power (W)		Current (A)	
		FLC	ANFIS	FLC	ANFIS
25	1000	450.5	560.1	36	45
25	800	424.94	430.2	33.9	36.81
25	600	342.07	345.49	27.4	27.63
25	400	230.48	234.69	18.43	18.72
25	200	105.71	107.93	8.46	8.63

### 3. Experimental Study of OSSCs with ANFISs

The samples of OSSCs are shown in Figure 21. The energy storage performances for each of the samples were made using 32 °C fluorescent lamps. The OSSC samples were preconditioned by short-circuiting the terminals for full depletion of the energy. Then, the OSSCs were tested under direct sunlight at an ambient temperature of 32 °C. A multimeter was attached to the output port of the ANFISs. Voltage and current readings were recorded at an interval of 1 s for 5 min.

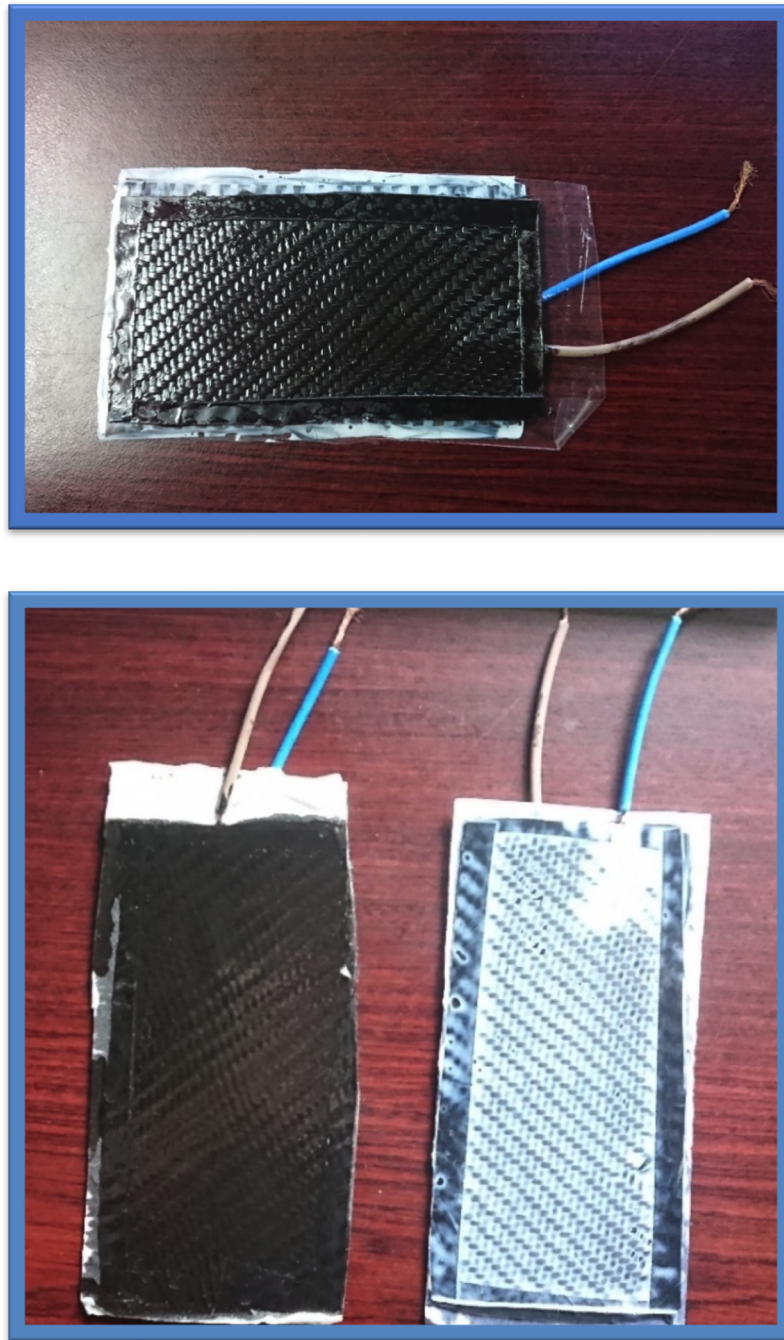


**Figure 21.** Organic solar cell with the composition of ZnO/CuO: AC.

The performance investigations of the OSSC both in charging and discharging modes were conducted at the time for the maximum values of state of charge (SoC)(t), W/kg, and energy density, W/A·h. Figure 22 shows the SoC(t) and state of discharge (SoD)(t) of the OSSC for different percentages of activated carbon (AC). It was noted that the wt% of ZnO for the P-type was kept constant but only the wt% of AC was changed. The result showed the difference both in charging and discharging for 6–20% of the AC. The higher percentage of AC particles increased the surface area and created more pores as well as utilising the PVDF polymer chains to wrap the CFs. However, the excessive percentage of AC

made the OSSC into a thin film and prevented the excitation of electron flow. Therefore, the OSSC can hold the charge for a longer time than the lower percentage of AC.

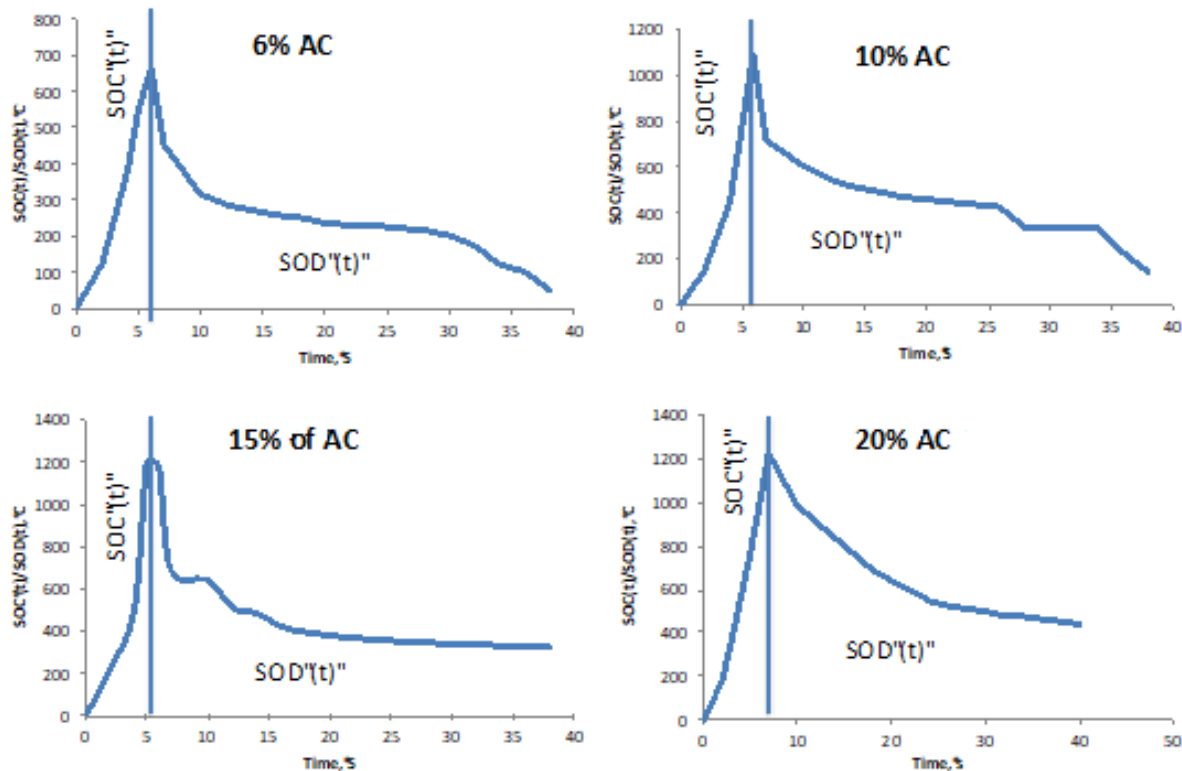


Figure 22. SoC(t) and SoD(t) at OSSC laboratory scale.

Figure 23a shows the power of 6.7 W/kg stored for 15% of AC OSSC at time = 5 s in charging while 1.8 W/kg for 20% of AC. It also indicated that if the OSSC size was made as 1 m<sup>2</sup>, it would be able to produce 65,000 W of power. It was not only able to meet the vehicle load demand but also able to charge the EV batteries with voltage 120 V and 540 A. However, an ANFIS will not allow for storing an OSSC such power. The high-power generation stored in an OSSC may be damaged due to heat gain. Figure 23b shows the power density of the OSSC, which was measured using the digital multimeter, both in charging and discharging. The result shows that the 15 wt% AC sample provided the highest power density of 3300 W/kg, and the 20 wt% AC sample produced the lowest power density of 2700 W/kg. This was due to the densely mixed AC which caused the micropore area to become a film, and it closed the interstitial space of the filler of ZnO with the PVDF. Figure 23c shows the energy density of the OSSC. The result showed that the highest energy density was 8.9 W·h/kg for the 15 wt% AC, and the lowest energy density was 1.7 W·h/kg for the 20 wt% AC. The summarised results of laboratory-scale OSSCs are presented in Table 12.

After 5 s of charging time, the OSSC with 15 wt% AC stored 6.7 W/kg of power and the OSSC with 20 wt% AC only stored 1.8 W/kg of power, as shown in Figure 23a. If the OSSC size increased to 1 m<sup>2</sup>, the power output was estimated to be 65,000 W. This amount of power was sufficient to provide charging for EV batteries with 120 V and 540 A. However, the ANFIS will control the power storage because the heat gain from high-power generation may cause damage to the storage devices.

The power density of the OSSCs was measured with a digital multimeter for both charging and discharging, as shown in Figure 23b. The OSSC with 15 wt% AC and 20 wt%

AC generated the highest power density (3300 W/kg) and the lowest power density (2700 W/kg), respectively. The high concentration of AC caused the micropores to become a thin film and filled the interstitial space of the filler ZnO with PVDF. Similarly, 15 wt% AC and 20 wt% AC produced the highest energy density (8.9 W·h/kg) and the lowest energy density (1.7 W·h/kg), respectively, as shown in Figure 23c. The summarised results of the laboratory-scale OSSCs are presented in Table 12.

**Table 12.** Overall performance of the AC-ZnO/CuO-ER\_CF EDLC.

AC (%)	Voltage ( $V_{oc}$ )	Capacitance C ( $\mu F/cm^2$ )	Current Density $J_{sc}$ ( $A/cm^2$ )	Power Density $P_{ms}$ (KW/kg)	Energy Density $E_{ms}$ (W·h/kg)
6	2.414	13.356	2.234	18.691	5.198
10	2.649	16.356	3.013	27.747	7.707
15	2.438	20.156	3.584	31.859	8.85
20	2.154	11.27	1.312	5.863	1.623

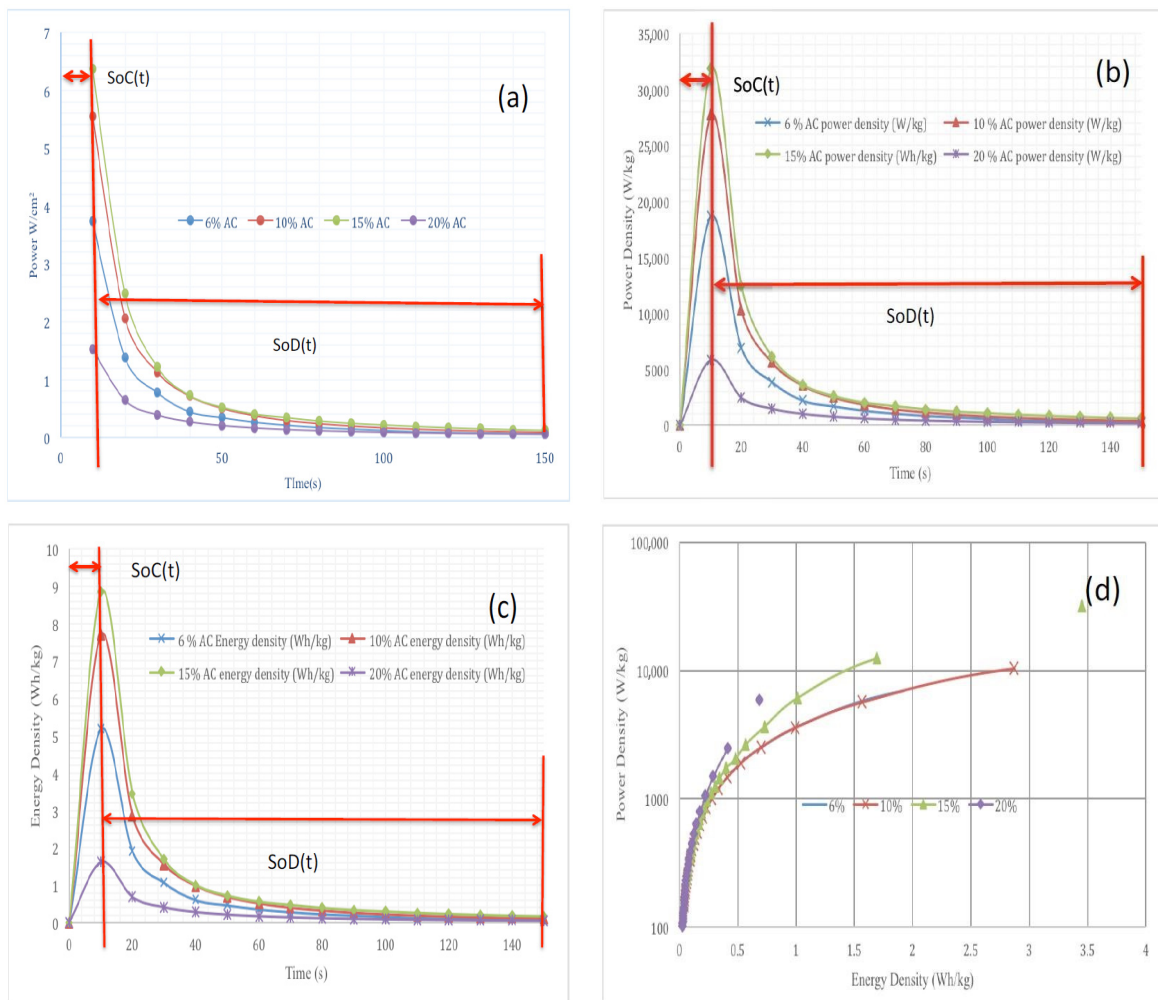


**Figure 23.** Performance of OSSC for the different % of AC (a–d).

#### 4. Conclusions

The conceptual OSSC laboratory-scale testing at solar temperature 32 °C can be summarised as below:

- The OSSC of a size of 2 m<sup>2</sup> has a solar energy conversion efficiency between 13–15%, power generation of 2800 W/day, a power density of 33 kW/kg, an energy density of 13 kW·h/kg, and capacitance of 11.17 µF/cm<sup>2</sup> at a temperature range of 25–32 °C and irradiance of 1000 W/m<sup>2</sup>.
- An OSSC for EVs is a promising, multifaceted structure that can reduce power consumption and emission due to its lightweight structure and reduction of traction.
- An ANFIS has produced better energy control compared to a PID controller and FLC using an OSSC at an irradiance of 1000 W/m<sup>2</sup> with an increase of 16% and 29%, respectively.
- The OSSC with a size of 1 m<sup>2</sup> produced a power of 65,000 W. It was not only able to meet the vehicle's electrical load demand but also able to charge the EV battery with a voltage of 120 V and 540 A. However, an ANFIS will not allow an OSSC to store high power.

For future research, an actual-size solar supercapacitor should be fabricated to be integrated with EVs. An ANFIS should be investigated with a commercialised solar supercapacitor for better efficiency and performance as well as integration with solar panels.

**Author Contributions:** Conceptualization, A.R.; Data curation, A.R. and K.M.A.; Investigation, A.R. and K.M.A.; Project administration, A.R.; Resources, A.R.; Software, A.R. and K.M.A.; Supervision, A.R.; Validation, A.R. and K.M.A.; Visualization, A.R. and K.M.A.; Writing—original draft, A.R., K.M.A., S.I., R.M.R.A.S., M.A.Q. and M.T.A.; Writing—review & editing, A.R., K.M.A., S.I., R.M.R.A.S., M.A.Q. and M.T.A. Funding acquisition, A.R. All authors have read and agreed to the published version of the manuscript.

**Funding:** This research was funded by Prototype Research Grants, Malaysia grant number PRGS22-023-0067.

**Data Availability Statement:** The data that support the findings of this study are available upon reasonable request from the authors.

**Acknowledgements:** The authors would like to thank the Office of Strategic Institutional Change (OSIC) of the International Islamic University Malaysia for their support of this project 'Flagship Project 2: Super-Fast Electric Vehicle Battery Charging System'.

**Conflicts of Interest:** The authors declare no conflict of interest.

#### References

1. Babalola, P.; Atiba, O. Solar powered cars—A review. *IOP Conf. Ser. Mater. Sci. Eng.* **2021**, *1107*, 012058. <https://doi.org/10.1088/1757-899X/1107/1/012058>.
2. Arulious, J.A.; Earlina, D.; Harish, D.; Priya, P.S.; Remy, A.I.; Mary, J.S.N. Design of solar powered electric vehicle. *J. Phys. Conf. Ser.* **2021**, *2070*, 012105. <https://doi.org/10.1088/1742-6596/2070/1/012105>.
3. Sarker, A.K.; Azad, A.K.; Rasul, M.G.; Doppalapudi, A.T. Prospect of Green Hydrogen Generation from Hybrid Renewable Energy Sources: A Review. *Energies* **2023**, *16*, 1556. <https://doi.org/10.3390/en16031556>.
4. Shah, R.M.R.A.; McGordon, A.; Rahman, M.; Amor-Segan, M.; Jennings, P. Characterisation of micro turbine generator as a range extender using an automotive drive cycle for series hybrid electric vehicle application. *Appl. Therm. Eng.* **2021**, *184*, 116302. <https://doi.org/10.1016/j.applthermaleng.2020.116302>.
5. Allafi, W.; Uddin, K.; Zhang, C.; Sha, R.M.R.A.; Marco, J. On-line scheme for parameter estimation of nonlinear lithium ion battery equivalent circuit models using the simplified refined instrumental variable method for a modified Wiener continuous-time model. *Appl. Energy* **2017**, *204*, 497–508. <https://doi.org/10.1016/j.apenergy.2017.07.030>.
6. Meng, H.; Li, Y.-F. A review on prognostics and health management (PHM) methods of lithium-ion batteries. *Renew. Sustain. Energy Rev.* **2019**, *116*, 109405. <https://doi.org/10.1016/j.rser.2019.109405>.
7. Kim, Y.-M.; Lee, J.-H.; Kim, S.-J.; Favrat, D. Potential and Evolution of Compressed Air Energy Storage: Energy and Exergy Analyses. *Entropy* **2012**, *14*, 1501–1521. <https://doi.org/10.3390/e14081501>.
8. Bezerra, M.L.H.; Zareipour, H., Six Days Ahead Forecasting of Energy Production of Small Behind-the-Meter Solar Sites. *Energies* **2023**, *16*, 1533. <https://doi.org/10.3390/en16031533>.
9. Parveen, N.; Ansari, S.A.; Ansari, M.Z.; Ansari, M.O. Manganese oxide as an effective electrode material for energy storage: A review. *Environ. Chem. Lett.* **2022**, *20*, 283–309. <https://doi.org/10.1007/s10311-021-01316-6>.

10. Rahman, A.; Rashid, M.; Mohiuddin, A.K.M.; Hawlader, M.N.A. Nano-Battery Technology for Ev-Hev Panel: A Pioneering Study. *IJUM Eng. J.* **2015**, *16*, 57–68. <https://doi.org/10.31436/iiumej.v16i2.604>.
11. Chen, H.; Lu, F.; Guo, F. Power management system design for small size solar-electric vehicle. In Proceedings of the 7th International Power Electronics and Motion Control Conference, Harbin, China, 2–5 June 2012; pp. 2658–2662. <https://doi.org/10.1109/IPEMC.2012.6259281>.
12. Li, Z.; Khajepour, A.; Song, J. A comprehensive review of the key technologies for pure electric vehicles. *Energy* **2019**, *182*, 824–839. <https://doi.org/10.1016/j.energy.2019.06.077>.
13. Ganji, B.; Kouzani, A.Z. A study on look-ahead control and energy management strategies in hybrid electric vehicles. In Proceedings of the IEEE ICCA 2010, Xiamen, China, 9–11 June 2010; pp. 388–392. <https://doi.org/10.1109/ICCA.2010.5524178>.
14. Shah, R.M.R.A.; Jones, R.P.; Cheng, C.; Picarelli, A.; Aziz, A.R.A.; Al Qubeissi, M. Model-Based Energy Path Analysis of Tip-In Event in a 2WD Vehicle with Range-Extender Electric Powertrain Architecture. *Energies* **2021**, *14*, 5696. <https://doi.org/10.3390/en14185696>.
15. Liu, Z.; Wang, Y.; Feng, J. Vehicle-type strategies for manufacturer’s car sharing. *Kybernetes* **2022**. <https://doi.org/10.1108/K-11-2021-1095>.
16. Clement, K.; Haesen, E.; Driesen, J. Coordinated charging of multiple plug-in hybrid electric vehicles in residential distribution grids. In Proceedings of the 2009 IEEE/PES Power Systems Conference and Exposition, Seattle, WA, USA, 15–18 March 2009; pp. 1–7. <https://doi.org/10.1109/PSCE.2009.4839973>.
17. Sawant, S.; Shah, R.M.R.A.; Rahman, M.; Aziz, A.R.A.; Smith, S.; Jumahat, A. System Modelling of an Electric Two-Wheeled Vehicle for Energy Management Optimization Study. *Evergreen* **2021**, *8*, 642–650. <https://doi.org/10.5109/4491656>.
18. Kötz, R.; Carlen, M. Principles and applications of electrochemical capacitors. *Electrochim. Acta* **2000**, *45*, 2483–2498. [https://doi.org/10.1016/S0013-4686\(00\)00354-6](https://doi.org/10.1016/S0013-4686(00)00354-6).
19. Burke, A. Ultracapacitors: Why, how, and where is the technology. *J. Power Sources* **2000**, *91*, 37–50. [https://doi.org/10.1016/S0378-7753\(00\)00485-7](https://doi.org/10.1016/S0378-7753(00)00485-7).
20. Geim, A.K.; Novoselov, K.S. The rise of graphene. *Nat. Mater.* **2007**, *6*, 183–191. <https://doi.org/10.1038/nmat1849>.
21. McDonough, J.R.; Choi, J.W.; Yang, Y.; La Mantia, F.; Zhang, Y.; Cui, Y. Carbon nanofiber supercapacitors with large areal capacitances. *Appl. Phys. Lett.* **2009**, *95*, 243109. <https://doi.org/10.1063/1.3273864>.
22. Xu, N.; Riley, J. Nonlinear analysis of a classical system: The double-layer capacitor. *Electrochem. Commun.* **2011**, *13*, 1077–1081. <https://doi.org/10.1016/j.elecom.2011.07.003>.
23. Gow, J.; Manning, C. Development of a photovoltaic array model for use in power-electronics simulation studies. *IEE Proc. - Electr. Power Appl.* **1999**, *146*, 193. <https://doi.org/10.1049/ip-epa:19990116>.
24. Huang, B.; Deng, H.-X.; Lee, H.; Yoon, M.; Sumpter, B.G.; Liu, F.; Smith, S.C.; Wei, S.-H. Exceptional Optoelectronic Properties of Hydrogenated Bilayer Silicene. *Phys. Rev. X* **2014**, *4*, 021029. <https://doi.org/10.1103/PhysRevX.4.021029>.
25. Andersen, T.R.; Dam, H.F.; Hösel, M.; Helgesen, M.; Carlé, J.E.; Larsen-Olsen, T.T.; Gevorgyan, S.A.; Andreasen, J.W.; Adams, J.; Li, N.; et al. Scalable, ambient atmosphere roll-to-roll manufacture of encapsulated large area, flexible organic tandem solar cell modules. *Energy Environ. Sci.* **2014**, *7*, 2925. <https://doi.org/10.1039/C4EE01223B>.
26. Bagher, A.M. Comparison of Organic Solar Cells and Inorganic Solar Cells. *Int. J. Renew. Sustain. Energy* **2014**, *3*, 53. <https://doi.org/10.11648/j.ijrse.20140303.12>.
27. Singh, U.; Rizwan, M. Analysis of Fuzzy Logic, ANN and ANFIS based Models for the Forecasting of Wind Power. In Proceedings of the 2018 2nd IEEE International Conference on Power Electronics, Intelligent Control and Energy Systems (ICPEICES), Delhi, India, 22–24 October 2018; pp. 1–7. <https://doi.org/10.1109/ICPEICES.2018.8897445>.
28. Yang, G.R.; Wang, X.-J. Artificial Neural Networks for Neuroscientists: A Primer. *Neuron* **2020**, *107*, 1048–1070. <https://doi.org/10.1016/j.neuron.2020.09.005>.
29. Jang, J.-S.R. ANFIS: Adaptive-network-based fuzzy inference system. *IEEE Trans. Syst. Man Cybern.* **1993**, *23*, 665–685. <https://doi.org/10.1109/21.256541>.

**Disclaimer/Publisher’s Note:** The statements, opinions and data contained in all publications are solely those of the individual author(s) and contributor(s) and not of MDPI and/or the editor(s). MDPI and/or the editor(s) disclaim responsibility for any injury to people or property resulting from any ideas, methods, instructions or products referred to in the content.